Motile cilia create fluid-mechanical microhabitats for the active recruitment of the host microbiome

Janna C. Nawroth[a,b,c,1], Hanliang Guo[d,1], Eric Koch[c], Elizabeth A. C. Heath-Heckman[e], John C. Hermanson[f], Edward G. Ruby[c], John O. Dabiri[b,g], Eva Kanso[d,2], and Margaret McFall-Ngai[c,2]

[a]Research & Development, Emulate Inc., Boston, MA 02210; [b]Graduate Aeronautical Laboratories and Bioengineering, California Institute of Technology, Pasadena, CA 91125; [c]Pacific Biosciences Research Center, University of Hawaii at Manoa, Honolulu, HI 96822; [d]Department of Aerospace and Mechanical Engineering, University of Southern California, Los Angeles, CA 90089-1191; [e]The Department of Molecular and Cell Biology, University of California, Berkeley, CA 94720; [f]US Department of Agriculture Forest Products Laboratory, Madison, WI 53726; and [g]Department of Civil and Environmental Engineering, Stanford University, Stanford, CA 94305

This contribution is part of the special series of Inaugural Articles by members of the National Academy of Sciences elected in 2014.

Contributed by Margaret McFall-Ngai, July 21, 2017 (sent for review April 26, 2017; reviewed by Christophe Eloy and M. A. R. Koehl)

We show that mucociliary membranes of animal epithelia can create fluid-mechanical microenvironments for the active recruitment of the specific microbiome of the host. In terrestrial vertebrates, these tissues are typically colonized by complex consortia and are inaccessible to observation. Such tissues can be directly examined in aquatic animals, providing valuable opportunities for the analysis of mucociliary activity in relation to bacteria recruitment. Using the squid–vibrio model system, we provide a characterization of the initial engagement of microbial symbionts along ciliated tissues. Specifically, we developed an empirical and theoretical framework to conduct a census of ciliated cell types, create structural maps, and resolve the spatiotemporal flow dynamics. Our multiscale analyses revealed two distinct, highly organized populations of cilia on the host tissues. An array of long cilia (∼25 μm) with metachronal beat creates a flow that focuses bacteria-sized particles, at the exclusion of larger particles, into sheltered zones; there, a field of randomly beating short cilia (∼10 μm) mixes the local fluid environment, which contains host biochemical signals known to prime symbionts for colonization. This cilia-mediated process represents a previously unrecognized mechanism for symbiont recruitment. Each mucociliary surface that recruits a microbiome such as the case described here is likely to have system-specific features. However, all mucociliary surfaces are subject to the same physical and biological constraints that are imposed by the fluid environment and the evolutionary conserved structure of cilia. As such, our study promises to provide insight into universal mechanisms that drive the recruitment of symbiotic partners.

cilia | microfluidics | host–bacterial symbiosis | biological fluid mechanics, biofiltration

Many eukaryotic cells feature motile cilia, microtubule-based surface actuators that sense and propel the extracellular fluidic environment (1–3). Whereas cilia and cilia-like structures that sort and capture bacteria or particles are common and well-characterized features of aquatic organisms (4–7), in terrestrial animals such as mammals, the internal location of ciliated surfaces has made them difficult to study. A central challenge in internal ciliated mucus membranes, such as those lining the fallopian tube, the Eustachian tube, and the respiratory system (8), is to reconcile the effective clearance of toxic molecules and undesirable microbes with selective engagement of beneficial symbionts. For example, on airway epithelia, the coordinated beat of motile cilia creates a horizontal flow across their tips (9–12), which clears mucus, microorganisms, and debris (Fig. 1*A*). Disruption of this mucociliary clearance can lead to chronic infection of the airways (13). However, this simple model is incomplete; ciliated airway epithelia not only serve a clearance function, but also provide a habitat and a gateway for coevolved symbionts that play an essential role in the development of the host immune system and are believed to provide colonization resistance against pathogens (14, 15). The mechanisms by which mucociliary epithelia cilia might facilitate such controlled discrimination, and hence provide a specific barrier function, remain unknown.

Here, based on a detailed empirical and computational case study, we describe a set of previously unrecognized mucociliary behaviors involved in selective bacterial recruitment. We propose that mucociliary epithelia are not restricted to homogeneous organization, but that cilia populations can vary in morphology, kinematics, and spatial distribution, giving rise to distinct fluid-mechanical microhabitats with transport functions that extend well beyond the cilia tips (Fig. 1*A*). In particular, we present an example of an internal mucociliary epithelium that facilitates recruitment of symbiotic bacteria by creating two well-defined flow fields: one that actively filters bacteria-sized particles from the ambient flow into a sheltered zone and another that provides the sheltered zone with enhanced diffusion, such that biochemical signaling between bacterial candidates and host epithelial cells may be facilitated.

Significance

Recent findings demonstrate that microbiome communities often reside on mucociliated surfaces. While mucociliary clearance of bacteria from such surfaces has been extensively studied, the process of bacterial recruitment has remained unexplored. Here, using a simple model system, we show that ciliated surfaces, in addition to their clearance function, can create fluid-mechanical microhabitats with distinct transport and mixing properties that facilitate the active recruitment of symbiotic candidates from a background of suspended particles. Although each specific system will have unique properties, because ciliary structure and function are highly conserved, studies of models will contribute to an understanding of rules governing the selective behavior of ciliated surfaces.

Author contributions: J.C.N., H.G., E.G.R., J.O.D., E. Kanso, and M.M.-N. designed research; J.C.N., H.G., and E. Kanso performed research; J.C.N., H.G., E. Kanso, and M.M.-N. contributed new reagents/analytic tools; J.C.N., E. Koch, E.A.C.H.-H., and J.C.H. conducted biological imaging; J.C.N., H.G., E.G.R., J.O.D., E. Kanso, and M.M.-N. analyzed data; and J.C.N., H.G., E.G.R., E. Kanso, and M.M.-N. wrote the paper.

Reviewers: C.E., Institut de Recherche sur les Phénomènes Hors Equilibre; and M.A.R.K., University of California, Berkeley.

Conflict of interest statement: Coauthor E.A.C.H.-H. and reviewer M.A.R.K. are both affiliated with the University of California, Berkeley, but in different departments.

See Profile on page 9494.

[1]J.C.N. and H.G. contributed equally to this work.

[2]To whom correspondence may be addressed. Email: kanso@usc.edu or mcfallng@hawaii.edu.

This article contains supporting information online at www.pnas.org/lookup/suppl/doi:10.1073/pnas.1706926114/-/DCSupplemental.

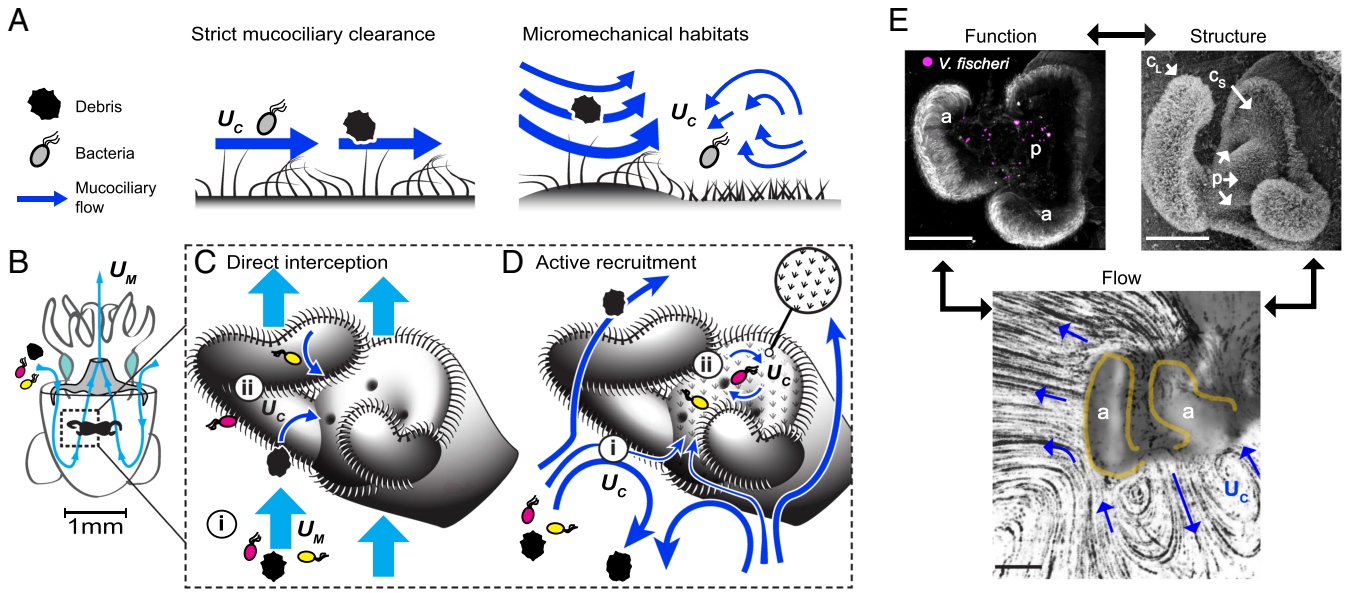

Fig. 1. Active recruitment of bacteria at mucociliary epithelia. (*A*, *Left*) Mucociliary flow with strict clearance function. (*A*, *Right*) Newly discovered mucociliary behaviors that can generate distinct flow regimes and micromechanical habitats. (*B*) *E. scolopes* inhales *V. fischeri* (magenta), and suspended material passes the paired internal mucociliary tissues (dotted box). (*C*) Model of direct interception (DI) of inhaled bacteria at the mucociliary surface (one side of paired organ shown). (*C*, *i*) Mantle-driven inhalation carries suspended matter past cilia. (*C*, *ii*) Matter is captured from flow by direct interception and transported to pores by mucociliary clearance. (*D*) Active recruitment mechanism. (*D*, *i*) Ciliary flow actively filters bacteria-sized particles into sheltered zone near pores where (*C*, *ii*) a structurally and behaviorally different population of cilia (*Inset*) enhances diffusion of biochemical signals. (*E*) Active recruitment mechanism was discovered by mapping the relationships between structure, function, and flow in the intact ciliated organ. Function: In vivo aggregation of bacterial symbiont *V. fischeri* (magenta) between appendages of ciliated organ before colonization. Structure: Scanning electron microscopy (SEM) image of the ciliated organ demarcates organization of two cilia populations. Flow: Black tracer path lines visualize cilia-driven flow with distinct vortical flow patterns below appendages (yellow outline). Blue arrows indicate flow direction. U_C, ciliary-driven flow; U_M, mantle-driven respiratory flow; *p*, pore; *a*, appendage; c_L, long cilia; c_S, short cilia. (Scale bars: 100 μm.)

We conducted our case study using the symbiosis between the squid *Euprymna scolopes* and the bioluminescent bacterium *Vibrio fischeri*, which is an established invertebrate model for investigating interactions between bacterial partners and their host epithelia (for review see ref. 16). Newly hatched *E. scolopes* recruit *V. fischeri* to the surface of their nascent light-emitting organ from inhaled seawater. The seawater, which contains a diverse background of other bacterial species and suspended abiotic particles, is drawn into the mantle cavity for the animal's respiratory flow and passes across the light organ. During embryogenesis, the light organ surface develops two complex, juvenile-specific ciliated fields—each featuring two appendages—that are lost after colonization by symbiotic bacteria, which indicates a possible role of the cilia in promoting symbiont recruitment (Fig. 1*B*). During initiation of symbiosis, *V. fischeri* cells become competitively dominant in bacterial aggregates located above the entry pores on the ciliated surface. They reside in these aggregates for a few hours, a time during which they become physiologically prepared or "primed" for their eventual migration through the pores and into the light organ (16). The strict timeline, well-defined localization, and exclusiveness of the squid–vibrio partnership, which occurs in an experimentally accessible, yet intact, internal organ, have revealed highly conserved biochemical mechanisms that also govern specific bacteria–host associations in mammals (16). Here, we used the squid–vibrio symbiosis to investigate the general question of how ciliary activity aids in the transport and selection of a bacterial partner to its target tissue. Specifically, we asked whether ciliary flow facilitates the recruitment of free-living *V. fischeri* cells from inhaled seawater and facilitates their engagement with the surface pores.

In the current model (17, 18), ciliary activity forms a conveyor belt of adhesive mucus, which directly intercepts particulates from the inhaled stream of seawater and moves them closer to the light organ's entry pores (Fig. 1*C*). Instead, we found that one population of cilia generated an outer, vortical flow zone extending far beyond the surface (~200–300 μm) and focusing bacteria and other micrometer-sized particles into an inner, sheltered zone near the surface pores, while preventing suspended matter from adhering elsewhere (Fig. 1*D*). In this zone, a second, structurally distinct population of cilia gently mixes the fluid, a behavior that could facilitate chemical signaling between host and bacteria (19) and, thereby, promote successful colonization of the light organ.

We discovered these mechanisms by following an integrated experimental and computational approach for dissecting the multiscale structure–function relationships that link the initiation of a bacteria–host association to both the cilia-generated flows and the structure of the ciliated tissues (Fig. 1*E*).

Results

Evidence for a Cilia-Mediated Bacteria–Host Association. Like the respiratory airways, the light organ is continuously exposed to inhaled particulate matter of a wide range of composition and size (20). In the early stages of symbiosis, wild-type *V. fischeri*, as well as nonmotile mutants of *V. fischeri*, nonsymbiont bacteria, and bacteria-sized synthetic particles, all accumulate at the light-organ surface (Fig. 1*E*), after which further selection takes place (17). These findings indicate that neither a specific bacteria shape nor a specific behavior is necessary for the first stage of association. This result poses two questions: (*i*) Does the respiratory flow directly deliver bacteria-sized particles to the ciliated surface? And (*ii*) how is larger particulate matter excluded from this surface?

Using video microscopy and particle tracking, we observed two counterrotating fluid vortices near the appendages of the light organ (Fig. 1*E*). These vortices occur in vivo as well as in excised

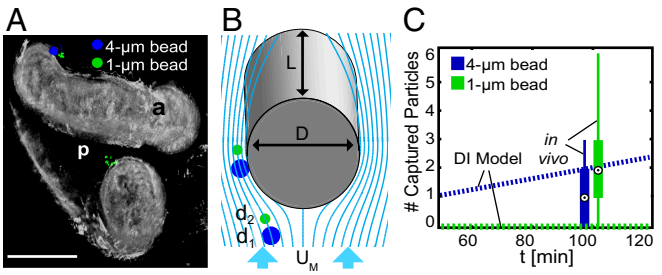

Fig. 2. The DI model fails to explain bacterial capture at the ciliated epithelium. (*A*) In vivo aggregation of bacteria-sized microbeads (1 μm diameter) on and between the appendages. Larger microbeads (4 μm diameter) are mostly excluded. *a*, appendage; *p*, pore. (Scale bar: 100 μm.) (*B*) Model of the DI mechanism where a cylindrical appendage captures particles from oncoming mantle-driven flow. d_1, d_2, particles with different diameters; *D*, *L*, diameter and length of appendage, respectively; U_M, respiratory flow. (*C*) Particle capture rates per ciliated field (with two appendages) for different particle sizes predicted by the DI model compared with those observed in vivo.

light organs, indicating little contribution of the mantle geometry in directing particle trajectories at this scale. Further, during respiration at rest, the mantle pulsates at a much lower frequency (2 Hz) than the ciliary beat frequency (10 Hz), producing a creeping flow that incrementally refreshes the fluid volume in the mantle but contributes negligible inertial mixing and is at least six times slower near the light organ than the cilia-generated surface flow (Fig. S1 and Movie S1). These observations raise the question of whether the mantle-driven flow could play a direct role in delivering suspended particles to the ciliated surface. Such particle capture from oncoming flow has been rigorously studied in aquatic suspension filter feeders (21–24). Mechanisms for particle capture include direct interception, inertial impaction, gravitational deposition, diffusion, and motile-particle deposition (5). We can rule out a dominant role of motile-particle deposition given that both motile and nonmotile particles are captured at similar timescales and locations (ref. 17 and Fig. 2*A*). Of the remaining mechanisms, direct interception (DI), where a particle follows a streamline approaching a solid structure at a distance equal to or less than the particle radius (Figs. 1*C* and 2*B*), would be dominant given the particle and flow properties observed in our system (*Model of Particle Capture by Direct Interception*) (25, 26).

To test experimentally whether DI could be a major mode of particle capture, we exposed the animals to a suspension containing both *V. fischeri*-sized (1 μm diameter) and larger (4 μm diameter) particles. We observed that 1-μm particles accumulated on the side of the appendages facing the pores, as previously reported (17), whereas the 4-μm particles tended to adhere to the outside of the appendages (Fig. 2*A*) and were captured at significantly lower rates (one-sided Wilcoxon rank sum test, $P = 0.013$; $n = 4$ animals and 7 pairs of ciliated appendages) (Fig. 2*C*). This size bias is consistent with a role of the light organ in retaining *V. fischeri* and rejecting larger suspended particulates. The DI model, however, predicts the opposite trend, i.e., a lower capture rate of *V. fischeri*-sized particles compared with larger particles (Fig. 2*C*) (27). Interestingly, impaired ciliary activity results in indiscriminate particle adhesion throughout the light-organ surface (Fig. S2). Together, these results suggest that particles are not captured by a passive, direct interception mechanism, but instead by an active, cilia-driven filtering mechanism that enables both clearance and selective, localized, aggregation of bacterial candidates at the ciliated surface. We next examined the structure, kinematics, and spatial organization of the cilia covering the surface and then quantitatively related these properties to the ciliary flows and filtering functions that emerged.

Structural and Kinematic Characterization of the Ciliated Epithelium. We used a rapid-fixation protocol, which "freezes" ciliary motion, followed by scanning electron microscopy (Fig. S3) to generate a snapshot image of ciliary activity on the light organ (28). We identified two distinct populations of cilia: long cilia beating in a metachronal wave along the outside of the appendages and short cilia with no detectable coordination covering the region around the pores and along the medial side of the appendages. High-speed video recordings (Movie S2) and confocal imaging, followed by kymograph analyses, ciliary beat frequency analysis, and kinematic analyses (Fig. 3 *A*–*J*), confirmed structural and kinematic differences between the two ciliary populations and enabled us to derive a tissue-wide map of spatiotemporal cilia organization and activity (Fig. 3*K*). The long cilia are 25 μm in length and exhibit a stereotypic movement

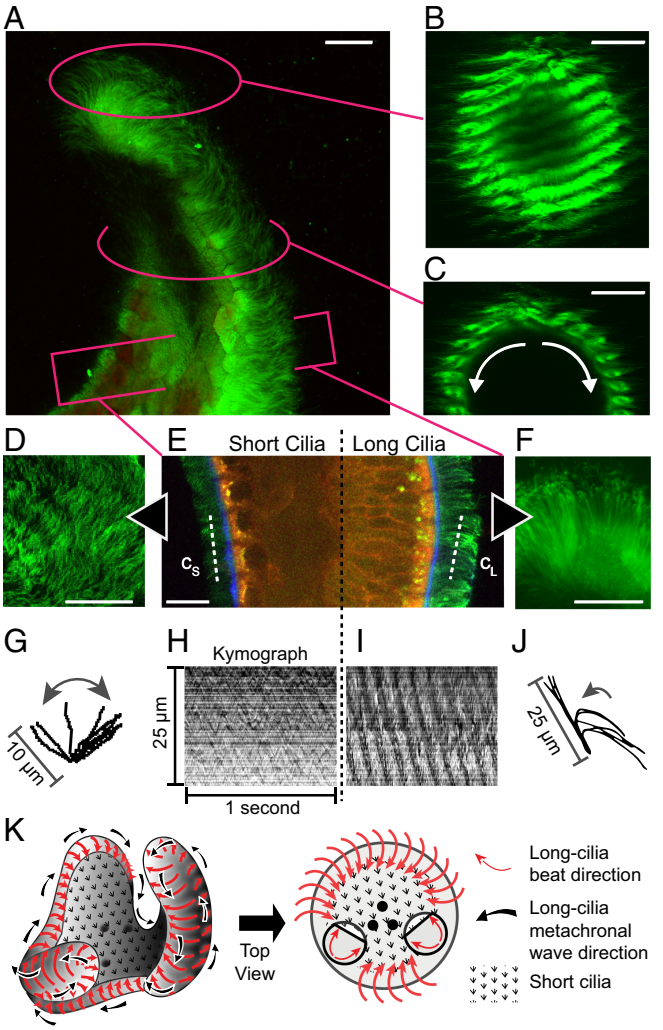

Fig. 3. Structural and kinematic characterization of the ciliated epithelium. (*A*) Live confocal imaging of a ciliated appendage. (*B*) Top view of appendage showing metachronal waves of the long cilia. (*C*) Cross-section of an appendage and metachronal waves. Arrows indicate direction of ciliary beating along the perimeter. (*D*) Close-up of short cilia. (*E*) Sagittal section of an appendage showing short (c_S) and long (c_L) cilia. Ciliary motion across dashed white lines is examined using kymography in panels *H* and *I*. (*F*) Close-up of long cilia. In *A*–*F*, cilia, green; cell membrane, red; mucus, blue. (Scale bars: 20 μm.) (*G*) Stroke-cycle kinematics of short cilia. Arrows indicate a bidirectional power stroke. (*H* and *I*) Typical cilia kymographs of short and long cilia, respectively. (*J*) Stroke-cycle kinematics of long cilia. Arrow indicates direction of power stroke. (*K*) Schematic of tissue-wide structural organization and beat kinematics of short and long cilia.

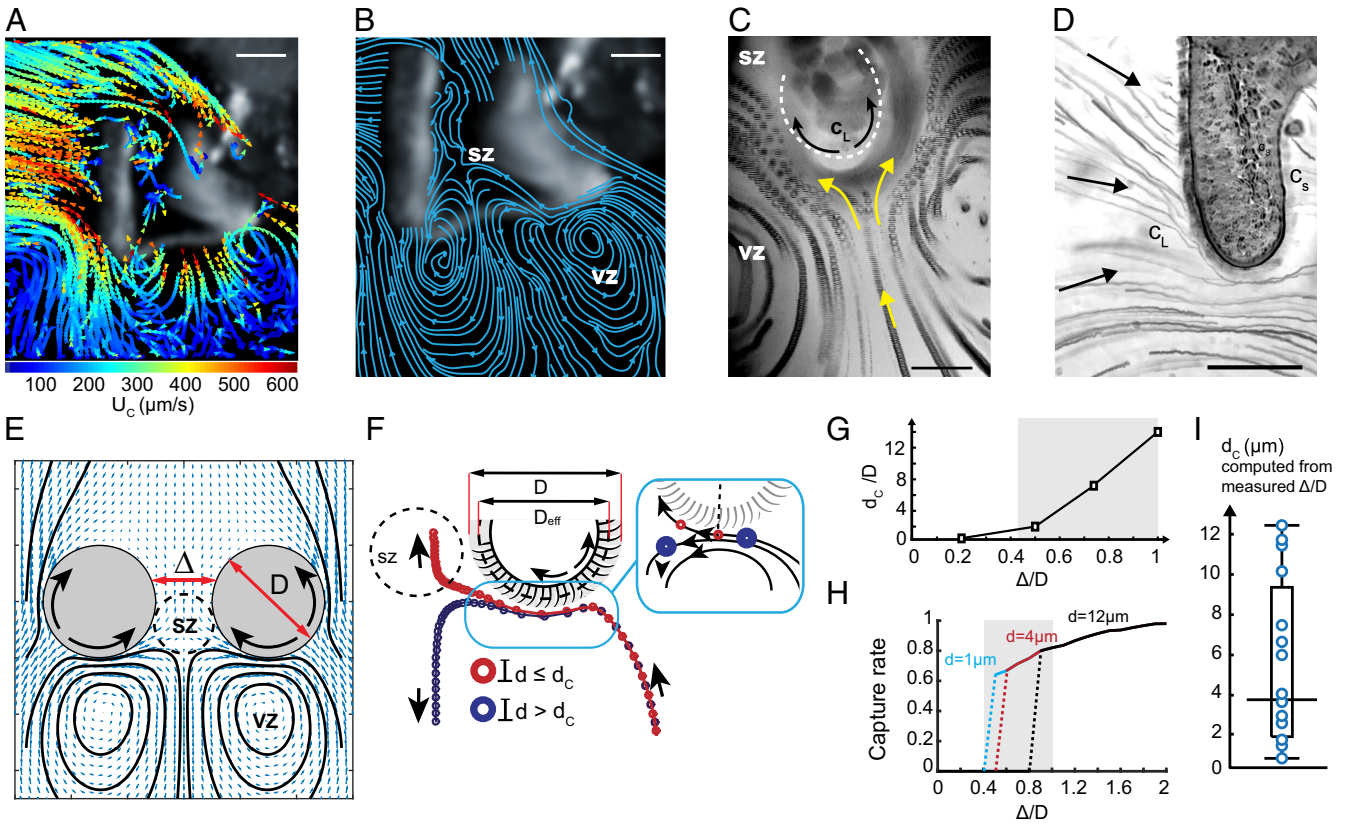

Fig. 4. Isolation of bacteria-sized particles by ciliary flow. (*A*) Ciliary flow velocities derived from particle-tracking velocimetry. (*B*) Streamlines computed from average flow velocity field, showing, like a traffic map, the path along which the fluid will flow at each location. (*C*) Cross-sectional flow around an appendage. (*D*) Side view of flow around appendage. (*E*) Computational flow field and streamlines generated by 2D model of ciliated appendages with diameter *D* and spacing of appendages Δ. Both vortical flow and sheltered zones are recreated by the model. (*F*) Computed trajectories of particles with different sizes. D_{eff}, diameter where fluid velocity boundary conditions are applied; *D*, diameter where particle–surface interactions begin. *Inset* (blue box) shows close-up of the size-selective streaming mechanism that sequesters particles below a critical particle diameter d_c into the sheltered zone. (*G*) Computed critical particle diameter d_c as a function of Δ/D. Gray box indicates empirically measured range of Δ/D. (*H*) Computed capture rate of particles with different diameters as a function of Δ/D. Gray box indicates empirically measured range of Δ/D. (*I*) Distribution of d_c values computed from empirically measured values of Δ. Longer horizontal line marks median value at 4 μm. c_L, long cilia; *sz*, sheltered zone; *vz*, vortical flow zone. (Scale bars: 80 μm.)

commonly seen in motile cilia, i.e., an asymmetric stroke pattern and metachronal coordination across neighboring cilia. In contrast, the short cilia are only 10 μm in length and display a temporally and spatially symmetric beat pattern that had no discernible coordination across neighboring cilia under any experimental condition. This unusual behavior is intriguing because, to our knowledge, symmetric and uncoordinated kinematics have been associated only with perturbed or pathological conditions (29, 30). Our data demonstrate that this behavior can occur in healthy conditions and may have been missed in other systems because of the focus on stereotypic structures and behaviors of motile cilia.

Long Cilia Help Select and Focus Bacteria-Sized Particles. Particle tracking and velocimetry in excised light organs revealed that the two populations of cilia generate two distinct flow compartments (Fig. 4 *A* and *B*, Fig. S4, and Movie S3): a vortical flow region consisting of two counterrotating vortices above the long cilia of the appendages and a sheltered zone near the pores above the short cilia. Both passive particles and motile *V. fischeri* cells that were caught in the vortices followed curved trajectories converging near the ciliated surface, where flow velocities reached up to 600 μm/s. Most of this entrained material was diverted into the central outward jet between the two vortices and was deflected away from the sheltered zone; however, a small fraction of particles entered and remained in the sheltered zone, often together with host-shed mucus (Movie S4). Moreover, the fast, near-surface flow generated by the long cilia prevented particle adhesion to the outer side of the appendages, while wrapping around and sheltering the zone lined by short cilia (Fig. 4 *C* and *D*), where particles were found to directly bind to the surface. We specifically verified that the vortical flow and deposition of *V. fischeri* and other small particles in the sheltered zone were not an artifact of removing the organ from the squid's mantle cavity, but also take place inside the intact, living animal (Fig. S5 and Movie S5). Further, captured bacteria that actively migrate out of the sheltered zone are swept away (31), which is consistent with the presence of two seamlessly interfacing compartments of slow and fast flows.

We used a computational model to probe the role of the long cilia in creating the two flow compartments. Namely, we reconstructed the cross-section of the organ's appendages by circumscribing the cilia tips, thereby producing two circles. We modeled the collective activity of the cilia by prescribing a tangential velocity around these circles that reflects the observed direction of the ciliary beat (Fig. 4*C*, Fig. S6 *A*–*F*, and Movie S6). This model does not take into account the beat pattern of the individual cilium; it rather accounts for the effective slip velocity caused by the ciliated surface. The resulting flow was obtained by solving Stokes equations for low-Reynolds numbers subject to the prescribed tangential velocities. This flow pattern recapitulates the cilia-driven flow observed empirically, i.e., a pair of

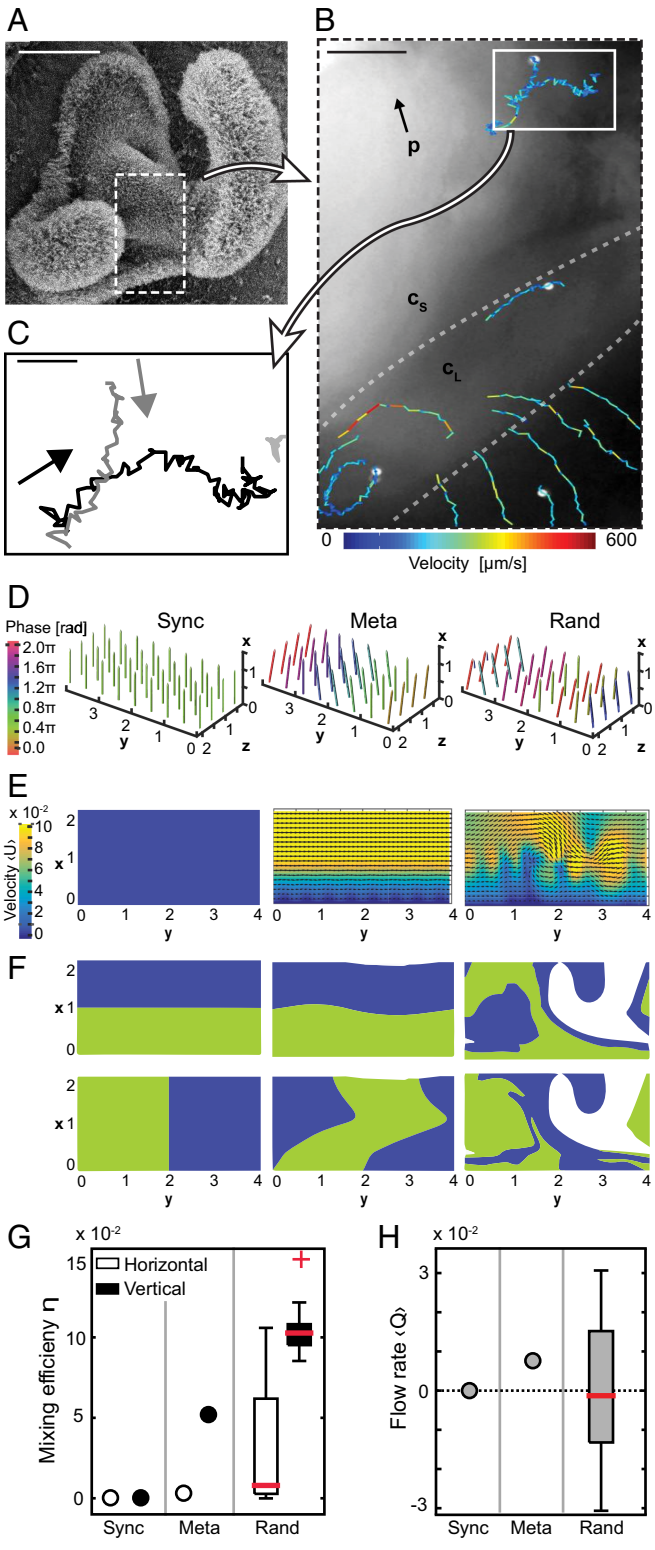

Fig. 5. Enhanced molecular mixing in the sheltered zone. (*A*) SEM of one of the two lateral surfaces of the ciliated organ. Dashed box indicates region where short and long cilia interface, as shown in detail in *B*. (Scale bar: 80 μm.) (*B*) Tracer trajectories visualize the two flow regimes created by long and short cilia. c_L, long cilia; c_S, short cilia; *p*, pore. (Scale bar: 25 μm.) (*C*) Close-up of tracer transport in a region of short cilia. The arrows indicate the starting direction of the tracked-particle tracer. (Scale bar: 5 μm.) (*D*) A computational model of fluid transport by a patch of cilia beating in synchrony (Sync), with metachronal wave (Meta), or with random phases between neighboring cilia (Rand). Shown are representative snapshots of each ciliary beating mode. Axes are normalized to cilia length. (*E*–*H*) For each mode, (*E*) average flow field over one beat cycle; (*F*) mixing of horizontally (*Top*) and vertically (*Bottom*) stratified particles after 16 beat cycles; (*G*) mixing efficiencies in the horizontal and vertical dimensions of different beat modes (box plots: results of 10 Monte Carlo simulations); and (*H*) average flow rates generated per cilium per beat cycle (box plots: results of 10 Monte Carlo simulations). In *G* and *H*, central rectangle spans first to third quartile of data, red line denotes median, "whiskers" show minimum and maximum, and red cross denotes outlier.

counterrotating vortices and a central sheltered zone (Fig. 4*E*). Although this flow pattern is robust to small perturbations in the tangential velocity profile, it is not necessarily reproducible by profiles corresponding to arbitrary ciliary beat patterns and spatial distributions (e.g., Fig. S6 *K*–*M*). This finding indicates that formation of the two distinct flow zones is sensitive to the spatiotemporal organization of ciliary beat.

Next, to explore whether the flow field constitutes a hydrodynamic sieve, selectively barring entrance of suspended material into the sheltered zone, we seeded the computed flow field with particles of finite diameter d that faithfully follow the flow streamlines (Fig. S6*G*). These particles model the transport of bacteria, which, under the flow condition given here, cross streamlines neither by diffusion nor by gravity or inertia because the bacteria are near neutrally buoyant (see *Flow Visualization and Analysis* and Table S1 for details). We observed size-selective streaming, wherein only particles up to a critical diameter d_c entered the sheltered zones (Fig. 4*F*). Particles larger than d_c span so many streamlines that they are diverted into the central outward jet, whereas smaller particles can follow the compressed near-surface streamlines into the sheltered zone. Interestingly, this mechanism has also been exploited in microfluidic devices for particle sorting (32, 33). We found that the value of d_c increases monotonically with the ratio of appendage spacing Δ and diameter D (Fig. 4*G*) because, for smaller ratios of Δ/D, there is greater convergence of outward-bound streamlines near the appendages, preventing any particles spanning these streamlines from entering the sheltered zone. Hence, for increasing ratios of Δ/D, particles of increasing diameter are captured, and the capture rate of all particles uniformly seeded across the span of the two appendages also increases (Fig. 4*H* and Fig. S6 *I*–*K*). For empirical ranges of Δ and D (Fig. S3), the model predicts a median value of $d_c = 4$ μm (Fig. 4*I*), which is congruent with the empirical outcomes. These results support our hypothesis of a cilia-driven selective mechanism that biases particle capture rates in favor of particles the size of bacterial symbionts.

Short Cilia Enhance Molecular Mixing. We next investigated the role of the short cilia lining the sheltered zones. Tracer trajectories suggested a mix of diffusive transport with crisscrossing directional flow (Fig. 5 *A*–*C* and Fig. S7); therefore, we speculated that the combination of symmetric beat kinematics in individual cilia and random stroke phase between neighboring cilia may result in enhanced fluid mixing, but no net transport. To test this hypothesis computationally, we developed a carpet model consisting of discrete cilia, where the beat kinematics of each cilium are adapted from empirical measurements (Fig. 2*G* and Fig. S8). We considered three modes of phase coordination: synchronous activity with no phase differences (SYNC), metachronal beating with a phase difference of 45° between neighboring cilia (META) (34), and random phase coordination, where each cilium is randomly assigned a phase between 0° and 360° (RAND) (Fig. 5*D*). Solving for the resulting flow fields, we found three distinct average patterns: specifically, zero net velocity in the SYNC mode, laminar flow in META mode, and vortical flow in RAND mode (Fig. 5*E*). To investigate the mixing performance of each flow field, we seeded horizontal or vertical strips of nondiffusing particle tracers (Fig. 5*F*) and let

this distribution of particles evolve during multiple cycles of ciliary beat. After 16 cycles, tracer distributions were strikingly different among the three cases: While there is no obvious pattern change in SYNC mode, and limited distortion in META mode, the RAND mode disrupts much of the initial stratification by stretching and folding fluid filaments, a hallmark of so-called chaotic mixing (35). To quantify mixing, we defined a mixing efficiency of $\eta_m = -\ln(m/m_0)/N_c$, where m_0 and m are the mixing numbers equivalent to the average minimum distance between tracer particles of different colors after 0 and N_c cycles, respectively (36, 37). Concordant with the qualitative results, the RAND mode outperforms the other modes in both horizontal and vertical mixing, with mixing efficiency depending on the particular phase distribution used in the simulation (Fig. 5*G*). Importantly, mixing in RAND mode predicts that initially neighboring particles quickly diverge on separate trajectories (Fig. S8), an expectation that matches the empirical data (Fig. 5*C*).

We then measured fluid transport in terms of volumetric flow rate Q, defined as the average volume of fluid moved per cilium per beat cycle (Fig. 5*H*). SYNC mode created zero net fluid transport, as expected from the Scallop theorem at low Reynolds numbers (38), while the META mode generated a small forward flow, and the RAND mode was equally likely to result in forward or backward flow, equivalent to a net flow rate near zero over time. It should be noted that the asymmetric beat generally associated with motile cilia will result in directional fluid transport in both the SYNC and RAND modes (39).

Taken together, these results suggest that a symmetric ciliary beat with a randomized phase achieves chaotic mixing that accelerates molecular transport without generating net fluid transport and effectively doubles the rate of diffusion of biochemical molecules in the kilodalton mass range (37). Such "enhanced" diffusion accelerates the formation of concentration gradients emanating from chemical signal sources, a mechanism exploited in microfluidic devices (40). Specifically, the characteristic time T to develop a steady-state gradient across a distance L is determined by diffusion rate D, with $T \sim L^2/(2D)$ (41). The faster spread and gradient formation of effector molecules would foster the biochemical dialogue among captured *V. fischeri* and between bacterial and host cells, including nitric oxide-mediated bacterial selection, chitobiose-dependent bacterial priming and chemotaxis, and the interaction with host-released antimicrobial molecules, including BPIs, lysozyme, PGRP2, and galaxin (16, 18). Indeed, a bacterial population in a well-mixed environment, i.e., with fully developed concentration gradients, can better initiate group behaviors by deducing bacterial cell density from the local concentration of quorum signals (42, 43).

Mixing without transport has not been previously described in common ciliary arrangements (34), demonstrating the importance of considering individual ciliary beat together with collective organization. In our analyses, it was first important to implement the symmetric stroke cycle, which by itself does not create any net flow because of the time reversibility in low-Reynolds number regimes (38) (Fig. S8). Second, because any flow-generating asymmetry must therefore arise from the activity of multiple cilia, it was necessary to recapitulate random-phase coordination among neighboring cilia. For the squid–vibrio system specifically, these findings add a fluid-mechanical dimension to the symbiont–host dialogue (Fig. S9), and they refute the longstanding assumption that flow generated by ciliary beat would necessarily compromise the formation of biochemical gradients for bacteria–host signaling (31). Taken together, our study has revealed a class of motile cilia with structural and kinematic adaptations that support fluid mixing in a stagnant zone and, hence, extend the known spectrum of ciliary functions.

Discussion

Our finding of different functional modalities of distinct cilia populations on mucus epithelia opens vistas for the understanding of these important subcellular structures in animal biology. It showcases how the impact of ciliated-tissue patterning extends well beyond the tissue surface, where it controls the formation of distinct fluid-mechanical environments. The combinatorial powers of ciliary parameters described in our study, such as beat direction, kinematics, and coordination, suggest a richness of potential scenarios for shaping the extracellular fluid environment at multiple scales to drive tissue homeostasis and remodeling, much as described for other tissue-organizing mechanical forces (44). Indeed, new imaging techniques have recently mapped both structurally distinct populations of cilia and spatiotemporally varying ciliary flow dynamics, in the ventricles of the mouse brain (45, 46). Multiscale analyses of ciliated tissues not only reveal new tissue-level phenomena, but also enable a quantification of their functional roles in different tissue environments. Such analyses require the integration of empirical and computational approaches for studying cilia function, like those developed in this study, as well as for investigating the particular fluid environment, including air and mucus (47).

In addition, our findings provide a mechanism by which ciliated epithelia generate a landscape of different fluid-mechanical microenvironments that support the formation of distinct "biogeographic" sites for the microbiota. Such a spatial series of ecological niches has previously been demonstrated along other epithelia, such as the mammalian gut lining, where tissue morphology and mucus interact to shape discrete microniches, each selecting for characteristic microbial communities important for gut function (48, 49). Furthermore, this study suggests how a microbial pathogen might alter ciliary movement to foster tissue colonization. These pathogens often misappropriate the mechanisms by which a host interacts with its beneficial bacteria, such as using the bacterial surface molecules lipopolysaccharide and peptidoglycan to signal the host (50). Here we have identified a distinct cilia-generated flow that creates a highly localized sheltered zone whose mechanical properties differ markedly from adjacent regions and in which bacterial cells accumulate. While the features of such biomechanical environments may have evolved to foster interaction with the beneficial microbiota, they may also be conscripted, or created de novo, by pathogens. For example, the human airway pathogen *Bordetella* spp. releases ciliostatic compounds, locally reducing ciliary beat and creating a micromechanical niche that favors pathogen attachment (51).

In conclusion, this study demonstrates that internalized ciliated epithelia can perform diverse and intricate fluid-transport tasks rivaling those of the externally ciliated surfaces of aquatic animals (7, 22, 52). Importantly, we have developed a theoretical and empirical framework for investigating the functional complexity of mucociliary epithelia. This framework will inform efforts to identify novel roles for cilia-generated flow and mechanical landscapes in human tissues and increase our appreciation of the functional scope of these important subcellular structures in animal biology.

Detailed methods and raw video recordings are available in *Supporting Information*.

ACKNOWLEDGMENTS. We thank B. Boettner, S. Fraser, and M. Kinzel for helpful discussion of the manuscript. Funding was provided by National Institutes of Health grants from The National Institute of Allergy and Infectious Diseases (AI050661) (to M.M.-N.) and Office of Research Infrastructure Programs (RR012294/OD011024) (to E.G.R.), by the Gordon & Betty Moore Foundation (3396) (to E.G.R.), and by a National Science Foundation Integrated NSF Support Promoting Interdisciplinary Research and Education Grant (NSF-MCB1608744) (to M.M.-N., E.G.R., and E. Kanso).

1. Choksi SP, Lauter G, Swoboda P, Roy S (2014) Switching on cilia: Transcriptional networks regulating ciliogenesis. *Development* 141:1427–1441.
2. Shah AS, Ben-Shahar Y, Moninger TO, Kline JN, Welsh MJ (2009) Motile cilia of human airway epithelia are chemosensory. *Science* 325:1131–1134.
3. Satir P, Christensen ST (2007) Overview of structure and function of mammalian cilia. *Annu Rev Physiol* 69:377–400.
4. Cheer AYL, Koehl MAR (1987) Paddles and rakes: Fluid flow through bristled appendages of small organisms. *J Theor Biol* 129:17–39.
5. Rubenstein DI, Koehl MAR (1977) The mechanisms of filter feeding: Some theoretical considerations. *Am Nat* 111:981–994.
6. Riisgard HU, Larsen PS (2001) Minireview: Ciliary filter feeding and bio-fluid mechanics–present understanding and unsolved problems. *Limnol Oceanogr* 46: 882–891.
7. Shapiro OH, et al. (2014) Vortical ciliary flows actively enhance mass transport in reef corals. *Proc Natl Acad Sci USA* 111:13391–13396.
8. Brooks ER, Wallingford JB (2014) Multiciliated cells. *Curr Biol* 24:R973–R982.
9. Fulford GR, Blake JR (1986) Muco-ciliary transport in the lung. *J Theor Biol* 121: 381–402.
10. Button B, et al. (2012) A periciliary brush promotes the lung health by separating the mucus layer from airway epithelia. *Science* 337:937–941.
11. Satir P, Sleigh MA (1990) The physiology of cilia and mucociliary interactions. *Annu Rev Physiol* 52:137–155.
12. O'Callaghan C, Sikand K, Rutman A (1999) Respiratory and brain ependymal ciliary function. *Pediatr Res* 46:704–704.
13. Knowles MR, Boucher RC (2002) Mucus clearance as a primary innate defense mechanism for mammalian airways. *J Clin Invest* 109:571–577.
14. Dickson RP, Erb-Downward JR, Huffnagle GB (2014) Towards an ecology of the lung: New conceptual models of pulmonary microbiology and pneumonia pathogenesis. *Lancet Respir Med* 2:238–246.
15. Gensollen T, Iyer SS, Kasper DL, Blumberg RS (2016) How colonization by microbiota in early life shapes the immune system. *Science* 352:539–544.
16. McFall-Ngai MJ (2014) The importance of microbes in animal development: Lessons from the squid-vibrio symbiosis. *Annu Rev Microbiol* 68:177–194.
17. Nyholm SV, Stabb EV, Ruby EG, McFall-Ngai MJ (2000) Establishment of an animal–bacterial association: Recruiting symbiotic vibrios from the environment. *Proc Natl Acad Sci USA* 97:10231–10235.
18. Kremer N, et al. (2013) Initial symbiont contact orchestrates host-organ-wide transcriptional changes that prime tissue colonization. *Cell Host Microbe* 14:183–194.
19. Altura MA, et al. (2013) The first engagement of partners in the *Euprymna scolopes-Vibrio fischeri* symbiosis is a two-step process initiated by a few environmental symbiont cells. *Environ Microbiol* 15:2937–2950.
20. Reynolds RA, Stramski D, Wright VM, Wożniak SB (2010) Measurements and characterization of particle size distributions in coastal waters. *J Geophys Res*115:C08024.
21. Labarbera M (1984) Feeding currents and particle capture mechanisms in suspension feeding animals. *Am Zool* 24:71–84.
22. Pepper RE, Roper M, Ryu S, Matsudaira P, Stone HA (2009) Nearby boundaries create eddies near microscopic filter feeders. *J R Soc Interface* 7:851–862.
23. Riisgård H, Larsen P (2010) Particle capture mechanisms in suspension-feeding invertebrates. *Mar Ecol Prog Ser* 418:255–293.
24. Cheer AYL, Koehl MAR (1987) Fluid flow through filtering appendages of insects. *Math Med Biol* 4:185–199.
25. Humphries S (2009) Filter feeders and plankton increase particle encounter rates through flow regime control. *Proc Natl Acad Sci USA* 106:7882–7887.
26. Shimeta J, et al. (1991) Physical mechanisms and rates of particle capture by suspension feeders. *Oceanogr Mar Biol Annu Rev* 29:l–257.
27. Nyholm SV, Deplancke B, Gaskins HR, Apicella MA, McFall-Ngai MJ (2002) Roles of *Vibrio fischeri* and nonsymbiotic bacteria in the dynamics of mucus secretion during symbiont colonization of the *Euprymna scolopes* light organ. *Appl Environ Microbiol* 68:5113–5122.
28. McFall-Ngai MJ, Ruby EG (1998) Sepiolids and vibrios: When first they meet. *BioScience* 48:257–265.
29. Nakhleh N, et al. (2012) High prevalence of respiratory ciliary dysfunction in congenital heart disease patients with heterotaxy. *Circulation* 125:2232–2242.
30. Werner ME, et al. (2011) Actin and microtubules drive differential aspects of planar cell polarity in multiciliated cells. *J Cell Biol* 195:19–26.
31. Mandel MJ, et al. (2012) Squid-derived chitin oligosaccharides are a chemotactic signal during colonization by Vibrio Fischeri. *Appl Environ Microbiol* 78:4620–4626.
32. Ahmed D, Mao X, Shi J, Juluri BK, Huang TJ (2009) A millisecond micromixer via single-bubble-based acoustic streaming. *Lab Chip* 9:2738–2741.
33. Karimi A, Yazdi S, Ardekani AM (2013) Hydrodynamic mechanisms of cell and particle trapping in microfluidics. *Biomicrofluidics* 7:021501.
34. Guo H, Nawroth J, Ding Y, Kanso E (2014) Cilia beating patterns are not hydrodynamically optimal. *Phys Fluids* 26:091901.
35. Jones SW, Thomas OM, Aref H (1989) Chaotic advection by laminar flow in a twisted pipe. *J Fluid Mech* 209:335–357.
36. Stone ZB, Stone HA (2005) Imaging and quantifying mixing in a model droplet micromixer. *Phys Fluids* 17:063103.
37. Ding Y, Nawroth J, McFall-Ngai M, Kanso E (2014) Mixing and transport by ciliary carpets: A numerical study. *J Fluid Mech* 743:124–140.
38. Purcell EM (1977) Life at low Reynolds number. *Am J Phys* 45:3–11.
39. Ding Y, Kanso E (2015) Selective particle capture by asynchronously beating cilia. *Phys Fluids* 27:121902.
40. Stroock AD, et al. (2002) Chaotic mixer for microchannels. *Science* 295:647–651.
41. Ahmed T, Shimizu TS, Stocker R (2010) Bacterial chemotaxis in linear and nonlinear steady microfluidic gradients. *Nano Lett* 10:3379–3385.
42. Cornforth DM, et al. (2014) Combinatorial quorum sensing allows bacteria to resolve their social and physical environment. *Proc Natl Acad Sci USA* 111:4280–4284.
43. Kim MK, Ingremeau F, Zhao A, Bassler BL, Stone HA (2016) Local and global consequences of flow on bacterial quorum sensing. *Nat Microbiol* 1:15005.
44. Heisenberg CP, Bellaïche Y (2013) Forces in tissue morphogenesis and patterning. *Cell* 153:948–962.
45. Liu T, Jin X, Prasad RM, Sari Y, Nauli SM (2014) Three types of ependymal cells with intracellular calcium oscillation are characterized by distinct cilia beating properties. *J Neurosci Res* 92:1199–1204.
46. Faubel R, Westendorf C, Bodenschatz E, Eichele G (2016) Cilia-based flow network in the brain ventricles. *Science* 353:176–178.
47. Vasquez PA, Jin Y, Palmer E, Hill D, Forest MG (2016) Modeling and simulation of mucus flow in human bronchial epithelial cell cultures – Part I: Idealized axisymmetric swirling flow. *PLoS Comput Biol* 12:e1004872.
48. Donaldson GP, Lee SM, Mazmanian SK (2016) Gut biogeography of the bacterial microbiota. *Nat Rev Micro* 14:20–32.
49. Kim HJ, Li H, Collins JJ, Ingber DE (2016) Contributions of microbiome and mechanical deformation to intestinal bacterial overgrowth and inflammation in a human gut-on-a-chip. *Proc Natl Acad Sci USA* 113:E7–E15.
50. Lebeer S, Vanderleyden J, De Keersmaecker SCJ (2010) Host interactions of probiotic bacterial surface molecules: Comparison with commensals and pathogens. *Nat Rev Microbiol* 8:171–184.
51. Anderton TL, Maskell DJ, Preston A (2004) Ciliostasis is a key early event during colonization of canine tracheal tissue by Bordetella bronchiseptica. *Microbiology* 150:2843–2855.
52. Jorgensen CB, Kiorboe T, Mohlenberg F, Riisgard HU (1984) Ciliary and mucus-net filter feeding, with special reference to fluid mechanical characteristics. *Mar Ecol Prog Ser* 15:283–292.
53. Montgomery MK, McFall-Ngai M (1993) Embryonic development of the light organ of the sepiolid squid Euprymna scolopes berry. *Biol Bull* 184:296–308.
54. Tropea C, Yarin AL (2007) *Springer Handbook of Experimental Fluid Mechanics* (Springer-Verlag GmbH, Berlin).
55. Schneider CA, Rasband WS, Eliceiri KW (2012) NIH image to ImageJ: 25 years of image analysis. *Nat Methods* 9:671–675.
56. Schindelin J, et al. (2012) Fiji: An open-source platform for biological-image analysis. *Nat Methods* 9:676–682.
57. Thielicke W, Stamhuis EJ (2014) PIVlab – towards user-friendly, affordable and accurate digital particle image velocimetry in MATLAB. *J Open Res Softw* 2:e30.
58. Tarantino N, et al. (2014) TNF and IL-1 exhibit distinct ubiquitin requirements for inducing NEMO–IKK supramolecular structures. *J Cell Biol* 204:231–245.
59. Benam KH, et al. (2016) Matched-comparative modeling of normal and COPD human airway responses to inhaled smoke in vitro. *Cell Syst* 3:456–466.
60. Cortez R (2001) The method of regularized Stokeslets. *SIAM J Sci Comput* 23: 1204–1225.
61. Ainley J, Durkin S, Embid R, Boindala P, Cortez R (2008) The method of images for regularized Stokeslets. *J Comput Phys* 227:4600–4616.
62. Eloy C, Lauga E (2012) Kinematics of the most efficient cilium. *Phys Rev Lett* 109:038101.
63. Miller CC (1924) The Stokes-Einstein law for diffusion in solution. *Proc R Soc A* 106:724–749.